# Geometric phase and bilayer cloak in macroscopic particle-diffusion systems

Liujun Xu,[1] Gaole Dai,[2] Gang Wang,[3,*] and Jiping Huang [1,†]

[1]*Department of Physics, State Key Laboratory of Surface Physics, and Key Laboratory of Micro and Nano Photonic Structures (MOE), Fudan University, Shanghai 200438, China*
[2]*School of Sciences, Nantong University, Nantong 226019, China*
[3]*School of Physical Science and Technology, Soochow University, Suzhou 215006, China*

Particle diffusion is a fundamental process in various systems, so its effective manipulation is crucially important. For this purpose, here we design a basic structure composed of two moving rings with equal-but-opposite velocities and a stationary intermediate layer, which can realize multiple functions to control particle diffusion. On the one hand, the intermediate layer allows particle exchange between the two moving rings, which gives birth to an exceptional point of velocity. As a result, a geometric phase appears for a loop evolution of velocity containing the exceptional point. On the other hand, the two moving rings also enhance the effective diffusivity of the intermediate layer, which helps design a bilayer particle-diffusion cloak. The present cloak only requires homogeneous parameters and simple structures, and meanwhile, its on and off can be flexibly controlled by velocity. These results broaden the scope of geometric phase and provide hints for designing particle-diffusion metamaterials.

## I. INTRODUCTION

Particle diffusion is a widespread transport method in porous media, electronic devices, and biochemical reactions, which has attracted lots of research interests. Many unexpected phenomena were revealed such as geometric phase [1,2] and diffusion diffraction [3,4]. Recently, the dominant equation of particle diffusion, i.e., the Fick law, has been proved to be form-invariant under coordinate transformations [5], yielding the development of particle-diffusion metamaterials [5–10]. In contrast to other diffusion systems like thermotics [11–15], more fundamental phenomena and mechanisms remain to be explored in particle-diffusion systems.

In this work, we design a basic structure which is composed of two moving rings with equal-but-opposite velocities connected by a stationary intermediate layer with permeability for particles (see the top inset of Fig. 1). This structure can be understood by a double-porosity model [16,17] to some extent. Actually, moving materials or time-dependent materials have attracted intensive research interests recently [18–22]. Li *et al.* [21] first revealed an exceptional point in a heat-diffusion system, which provides a direct guidance for the exceptional point in our particle-diffusion system. Going beyond the exceptional point, we further reveal a geometric phase and bilayer cloak in this work. Therefore, although the present structure is similar to that adopted for heat-diffusion systems in Ref. [21], we reveal more physics including the geometric phase and bilayer cloak, and may provide potential applications for chemical reactions, fuel cells, drug delivery, catalysis, etc. Let us understand this structure from two aspects.

On the one hand, the intermediate layer makes the two moving rings coupled together, which can be effectively described by a non-Hermitian Hamiltonian. As a result, an exceptional point of velocity exists. If the velocity exceeds the exceptional point, a stationary concentration profile will turn into a moving one due to the broken of anti-parity-time symmetry [21–27] (see the left inset of Fig. 1). To go further, we also explore a cyclic path of time-varying velocity containing the exceptional point, which can give birth to an extra phase difference of $\pi$ (say, geometric phase). A schematic diagram can be seen in the bottom inset of Fig. 1.

On the other hand, the two moving rings also affect the intermediate layer. That is, the effective diffusivity of the intermediate layer is largely enhanced, which is beneficial to design a bilayer particle-diffusion cloak. Compared with existing mechanisms based on the transformation theory or multilayered structures [5–10], our scheme only requires homogeneous parameters and simple structures, which is convenient for practical applications.

## II. GEOMETRIC PHASE

The particle-diffusion process in the top inset of Fig. 1 can be effectively described by a non-Hermitian Hamiltonian $\boldsymbol{H}$,

$$\boldsymbol{H} = \begin{bmatrix} -\mathrm{i}(k^2 D + h) + ku & \mathrm{i}h \\ \mathrm{i}h & -\mathrm{i}(k^2 D + h) - ku \end{bmatrix}, \quad (1)$$

where $k$ is wave number, $D$ is the diffusivity of the two moving rings, $u$ is velocity, and $\mathrm{i} = \sqrt{-1}$ is the imaginary unit. The coefficient $h = D_m/(w\,d)$ reflects the exchange rate of particles between the two moving rings, where $D_m$ and

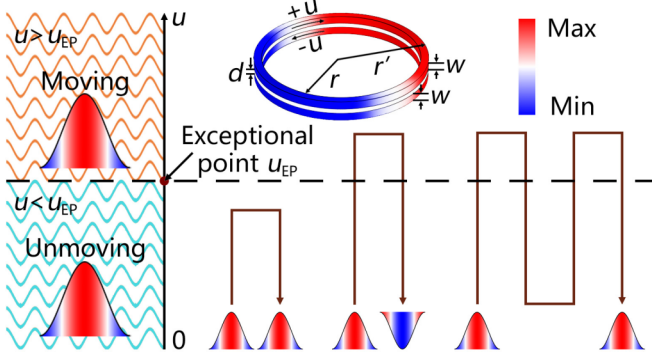*phwanggang@gmail.com
†jphuang@fudan.edu.cn

FIG. 1. Schematic diagram of geometric phase. The model is shown on top, which involves two moving rings separated by a permeable layer. Dependent on the velocity $u$, concentration profiles can be unmoving or moving. After a cyclic path in the velocity space, the particle concentration (shown with reference to the color bar in the upper-right corner) may return to the initial state with or without a $\pi$-phase shift.

$w$ are, respectively, the diffusivity and thickness of the two moving rings, and $d$ is the thickness of the intermediate layer. Detailed derivations of Eq. (1) can be found in the Appendix. The eigenvalues of the $\boldsymbol{H}$ are

$$\omega = -\mathrm{i}[(k^2 D + h) \pm \sqrt{h^2 - k^2 u^2}], \tag{2}$$

where $\omega$ is complex frequency. $u_{\mathrm{EP}} = h/k$ is an exceptional point of velocity. The eigenstates for $u < u_{\mathrm{EP}}$ are

$$\boldsymbol{\psi}_+ = [1, \ \mathrm{e}^{\mathrm{i}(\pi - \theta)}]^{\mathrm{T}}, \quad \boldsymbol{\psi}_- = [1, \ \mathrm{e}^{\mathrm{i}\theta}]^{\mathrm{T}}, \tag{3}$$

where $\theta = \sin^{-1}(ku/h)$, and T denotes transpose. The eigenstates for $u > u_{\mathrm{EP}}$ are

$$\boldsymbol{\psi}_+ = [\mathrm{e}^{-\phi}, \ \mathrm{e}^{\mathrm{i}\pi/2 - 2\phi}]^{\mathrm{T}}, \quad \boldsymbol{\psi}_- = [\mathrm{e}^{-\phi}, \ \mathrm{e}^{\mathrm{i}\pi/2}]^{\mathrm{T}}, \tag{4}$$

where $\phi = \cosh^{-1}(ku/h)$. Eigenvalues and eigenstates are plotted in Fig. 7 of the Appendix.

Then, we can check that the non-Hermitian Hamiltonian $\boldsymbol{H}$ satisfies $\boldsymbol{H}^\dagger \overline{\boldsymbol{\psi}}_\pm = \overline{\omega}_\pm \overline{\boldsymbol{\psi}}_\pm$, where $\boldsymbol{H}^\dagger$ is the Hermitian transpose of $\boldsymbol{H}$. $\overline{\boldsymbol{\psi}}_\pm$ and $\overline{\omega}_\pm$ are the complex conjugate of $\boldsymbol{\psi}_\pm$ and $\omega_\pm$, respectively. The eigenstates also satisfy $\langle \overline{\boldsymbol{\psi}}_\pm, \boldsymbol{\psi}_\mp \rangle = 0$, where $\langle \overline{\boldsymbol{\psi}}_\pm, \boldsymbol{\psi}_\mp \rangle$ denotes the complex inner product of $\overline{\boldsymbol{\psi}}_\pm$ and $\boldsymbol{\psi}_\mp$. Considering a time-varying velocity $u$, we can write down the complex geometric phase under adiabatic approximation as [28]

$$\gamma_\pm = \mathrm{i} \int \frac{\langle \overline{\boldsymbol{\psi}}_\pm(u), d\boldsymbol{\psi}_\pm(u) \rangle}{\langle \overline{\boldsymbol{\psi}}_\pm(u), \boldsymbol{\psi}_\pm(u) \rangle}, \tag{5}$$

which agrees with the result of non-Hermitian quantum systems. The exceptional point yields $\langle \overline{\boldsymbol{\psi}}_\pm(u_{\mathrm{EP}}), \boldsymbol{\psi}_\pm(u_{\mathrm{EP}}) \rangle = 0$ due to the coalescence of two eigenstates. Therefore, the exceptional point serves as a pole in the complex integral. We can rewrite Eq. (5) in a closed loop around the exceptional point as [29]

$$\gamma_\pm = \frac{\mathrm{i}}{2} \oint d \ln \langle \overline{\boldsymbol{\psi}}_\pm(u), \boldsymbol{\psi}_\pm(u) \rangle. \tag{6}$$

The geometric phase takes on $\gamma_\pm = \pi$ or $-\pi$ according to the residue theorem, and the sign is determined by the direction

of closed loop. If the evolution route does not contain the exceptional point, the integral in a closed loop is naturally equal to zero.

To physically understand the origin of geometric phase, we also discuss the dynamics from noneigenstates to eigenstates with COMSOL MULTIPHYSICS (http://www.comsol.com/). We define $C_1$ and $C_2$ as the concentrations along the upper and lower interior edges of the moving rings. The initial states are set at five eigenstates with the forms in the Cartesian coordinates as $C_1(x, y, t = 0) = A_1 y / \sqrt{x^2 + y^2} + B_1$ and $C_2(x, y, t = 0) = A_2 (y / \sqrt{x^2 + y^2} \cos\theta - x / \sqrt{x^2 + y^2} \sin\theta) + B_2$ for $\omega_-$ [or $C_2(x, y, t = 0) = A_2 (-y / \sqrt{x^2 + y^2} \cos\theta - x / \sqrt{x^2 + y^2} \sin\theta) + B_2$ for $\omega_+$] with $A_1 = A_2 = 200$, $B_1 = B_2 = 300$, and $\theta = \sin^{-1}(ku/h)$. Then, we set velocities at 100 ($< u_{\mathrm{EP}}$) and 300 ($> u_{\mathrm{EP}}$) $\mu$m/s to study evolutions. The directions of velocity are clockwise for the upper ring and anticlockwise for the lower ring. The theoretical phase differences with $u = 100$ $\mu$m/s are $\pi/6$ for $\omega_-$ and $5\pi/6$ for $\omega_+$. We track the evolutions of $C_1$ and $C_2$ by following their maximum points. The initial and final states are shown in the left column of Fig. 2. The trajectories of Max($C_1$) and Max($C_2$) with two different velocities are plotted in the right two columns of Fig. 2.

Since the initial states are not the eigenstates of $u = 100$ $\mu$m/s, these noneigenstates start moving to eigenstates. Finally, all five initial states move to the same final state with $\theta \approx \pi/6$, which is the eigenstate of the eigenvalue $\omega_-$. This occurs because of the nonorthogonality of the two eigenstates at different branches (for example, the eigenstates $\mathrm{E}_1^+$ and $\mathrm{E}_2^-$ are not orthogonal) [21]. Meanwhile, the decay rate of the upper branch is much lager than that of the lower one, so the eigenstate at the lower branch becomes the final observable one associated with the eigenvalue $\omega_-$.

In addition to the final states, we also care about evolution routes. For example, the moving directions of maximum point in Figs. 2(h), 2(k), and 2(n) are all against the velocities of respective moving rings. This occurs because the evolution route should try to avoid going through the eigenstate of the eigenvalue $\omega_+$ (with a far larger decay rate) to survive longer. A principle is to ensure concentration profiles to survive as long as possible. When the velocity is larger than the exceptional point, the concentration profiles are always moving because the real parts of eigenvalues $\omega$ appear (see the right column in Fig. 2).

We also perform finite-element simulations to visualize geometric phase. We consider a cyclic path of velocity excluding the exceptional point. The initial velocity is $u = 100$ $\mu$m/s, and the initial state is set at the eigenstate associated with $\omega_-$ (say, a phase difference of $\pi/6$). Then, we evolve the velocity according to the curve shown in Fig. 3(a). In this process, the eigenvalue is always purely imaginary, indicating that no extra phase difference is accumulated. As a result, this path brings the final state back to the initial concentration profile exactly [see Figs. 3(b) and 3(c)].

However, it is different when the path of velocity contains the exceptional point [see Figs. 3(d)–3(f) and Figs. 3(g)–3(i)]. As the velocity increases and exceeds the exceptional point, the real parts of eigenvalues appear, indicating that an extra
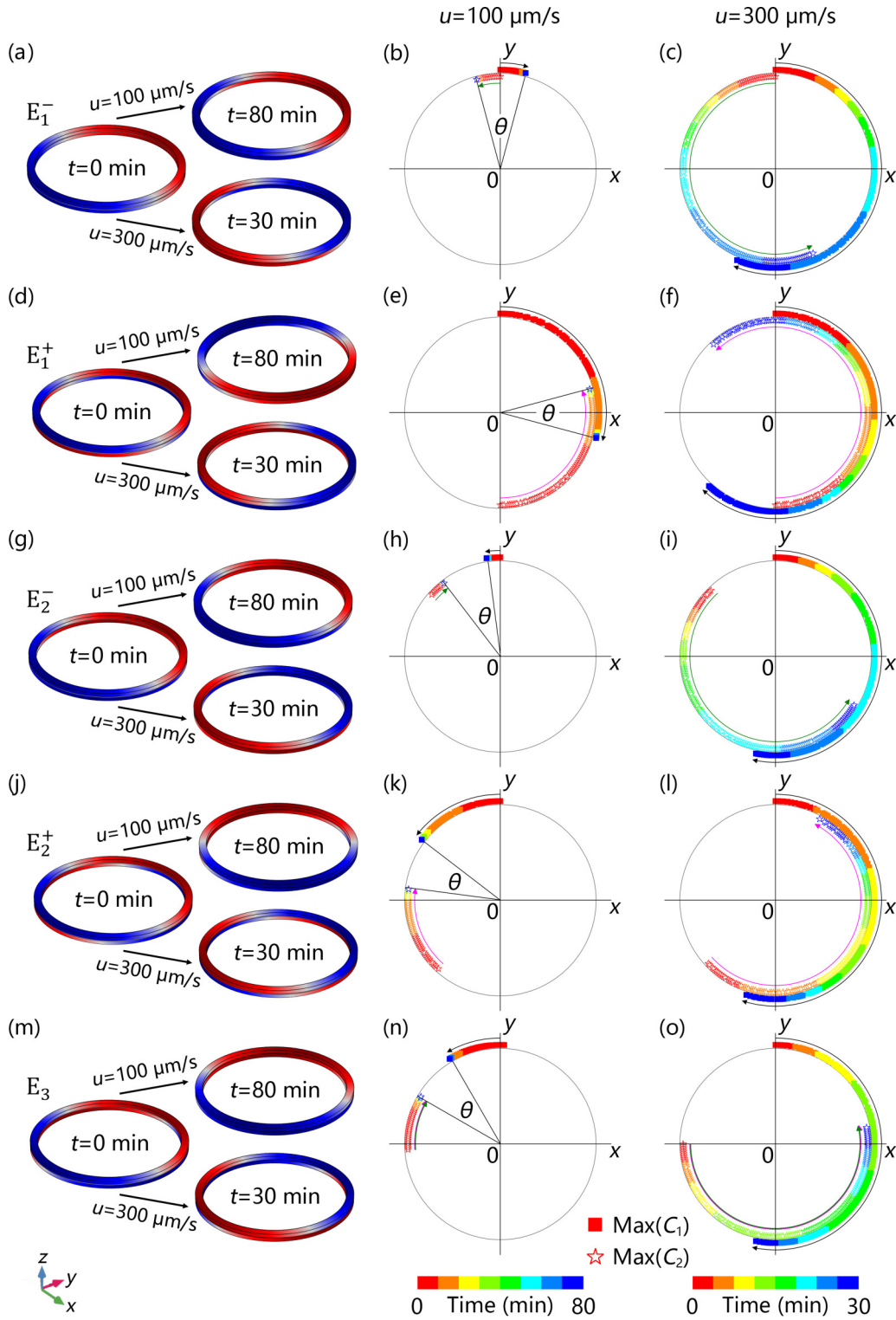
FIG. 2. Evolution of eigenstates. The initial and final states with two different velocities are presented in the left column. The trajectories of $\text{Max}(C_1)$ and $\text{Max}(C_2)$ along the interior edges of the two moving rings with $u = 100$ and $u = 300$ $\mu$m/s are shown in the middle and right columns, respectively. Parameters: $w = 0.5$ cm, $d = 0.1$ cm, $r = 10$ cm, $r' = 11$ cm, $D = 10^{-6}$ m$^2$/s, and $D_m = 10^{-8}$ m$^2$/s.

phase difference starts to accumulate. This process smoothly brings the initial state from one branch to the other. When the accumulated phase difference makes the state go through the eigenstate of another eigenvalue $\omega_+$ (with a phase difference

of $5\pi/6$), the profile can no longer go back to the initial position, as discussed in Fig. 2. Then, the phase difference continuously increases to reach a different position associated with eigenvalue $\omega_-$ and phase difference $\pi/6$. Fortunately, the
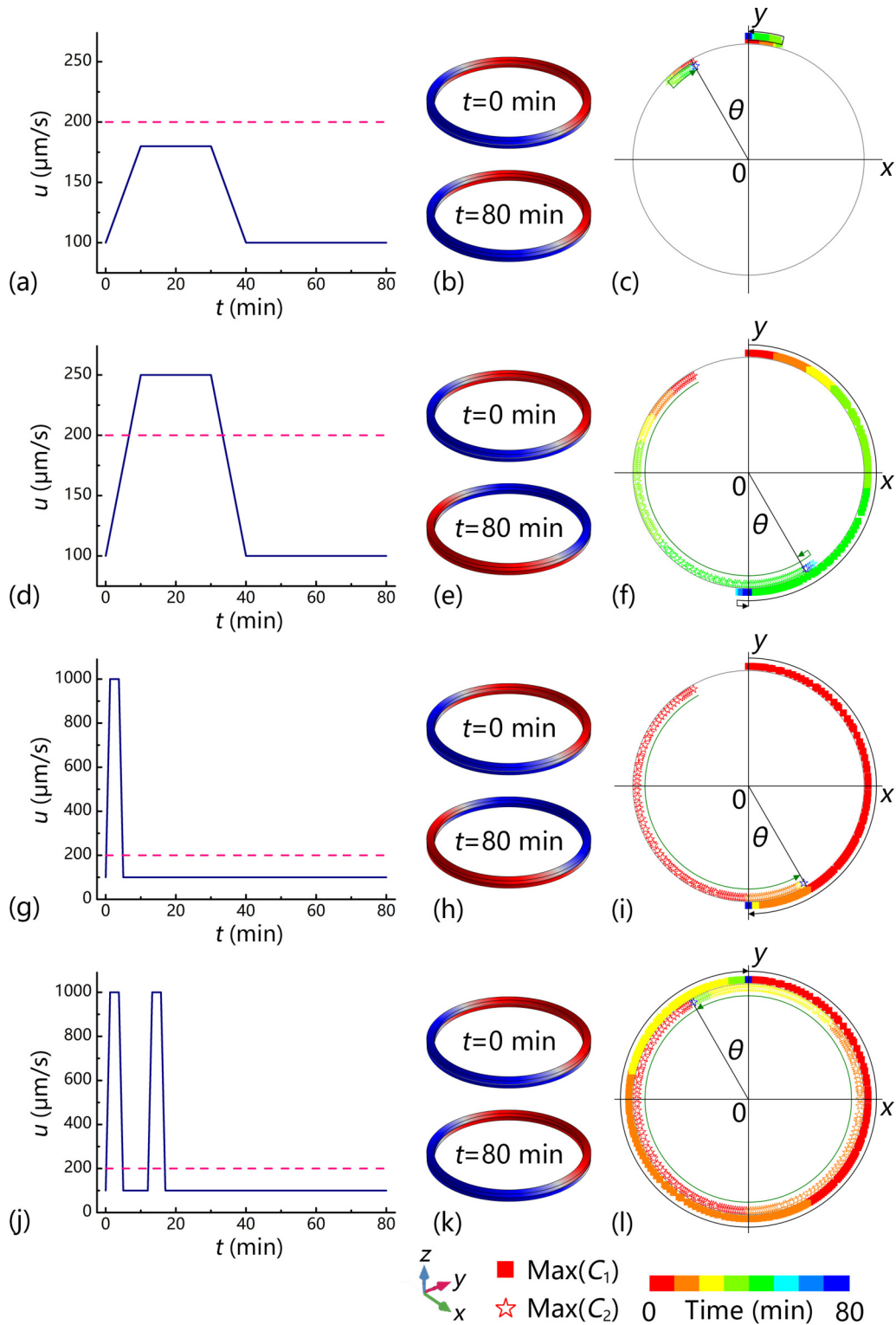
FIG. 3. Simulations of geometric phase. The left column describes the paths of time-varying velocity. The middle column shows the initial and final states. The right column illustrates the trajectories of Max($C_1$) and Max($C_2$) along the interior edges of the channels. The parameters are the same as those for Fig. 3.

concentration profile is flipped after one loop, and a phase difference of $\pi$ is accumulated [see Figs. 3(e) and 3(f), and Figs. 3(h) and 3(i)]. This is just the indicator of geometric phase. Here, the eigenstate $\psi_+$ has a geometric property to some extent.

Finally, when the cyclic evolution goes cross the exceptional point twice [see Fig. 3(j), say, crossing the eigenstate corresponding to the eigenvalue $\omega_+$ twice], it brings back to the initial state without any global phase change [see Figs. 3(k) and 3(l)].
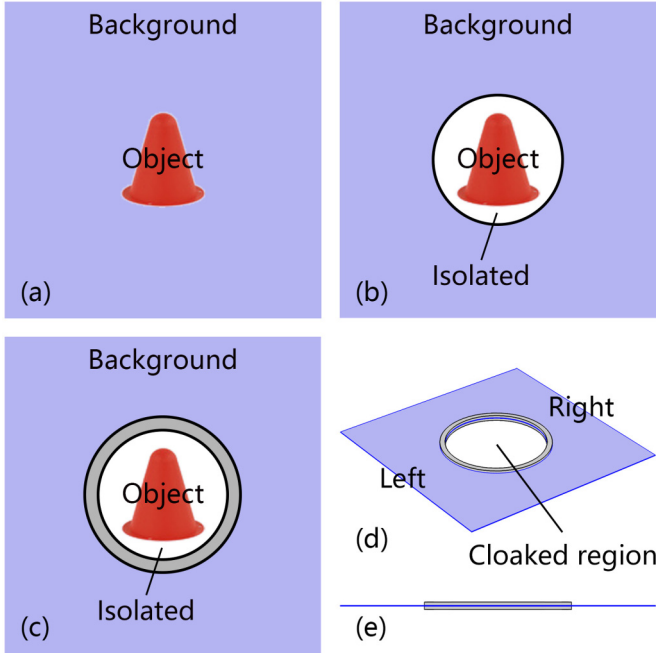
FIG. 4. Schematic diagram of bilayer particle-diffusion cloak. (a) Object in the background. (b) Separating the object and background with an isolated (zero-diffusivity) layer. (c) Applying two moving rings with appropriate velocity. (d) and (e) Three-dimensional views.



FIG. 5. Cloaking effect in a linear field. The square plate is $44 \times 44 \times 0.1$ cm$^3$ with diffusivity of $10^{-6}$ m$^2$/s. The two moving rings are with $w = 0.5$ cm and $D = 10^{-8}$ m$^2$/s. (a) Square object with width of 12 cm and diffusivity of $10^{-4}$ m$^2$/s in the center. (b) Isolated hole with radius of 10 cm in the center. (c) Two rings with inner radius of 10 cm and outer radius of 11 cm in the center, moving with equal-but-opposite velocities of 37 $\mu$m/s. (d) Pure background.

## III. BILAYER CLOAK

We have discussed the effect of the intermediate layer on the two moving rings, i.e., allowing particle exchange. In this part, we discuss from another aspect, i.e., the effect of the two moving rings. That is, the moving of the two rings enhances the effective diffusivity of the intermediate layer, which is helpful to design a bilayer particle-diffusion cloak. Cloaking is one of the most attractive functions which can protect objects from being detected. Particle-diffusion cloaking has also potential applications in chemical and biological systems.

The design idea is schematically shown in Fig. 4. When there is an object in the background, the concentration profile will be distorted [see Fig. 4(a)]. Then, we apply two steps to remove concentration distortion. Firstly, we use a layer with zero diffusivity to make the object isolated [see Fig. 4(b), forming a cloaked region], so the object can no longer affect the background. Secondly, we add another layer composed of two moving rings to remove the negative effect of isolated region [see Fig. 4(c)]. By adjusting the equal-but-opposite velocity appropriately, particle-diffusion invisibility can be achieved. The three-dimensional views are presented in Figs. 4(d) and 4(e). Since we use two layers (one layer for isolation and another one for compensation), the cloak is also called a bilayer cloak.

The simulations with a linear field is shown in Fig. 5. The left and right sides are fixed at high and low concentrations, respectively. The other two sides are associated with no-flux conditions. When there is a square object in the center, the isolines are repelled [see Fig. 5(a)]. When we use the first layer to isolate the object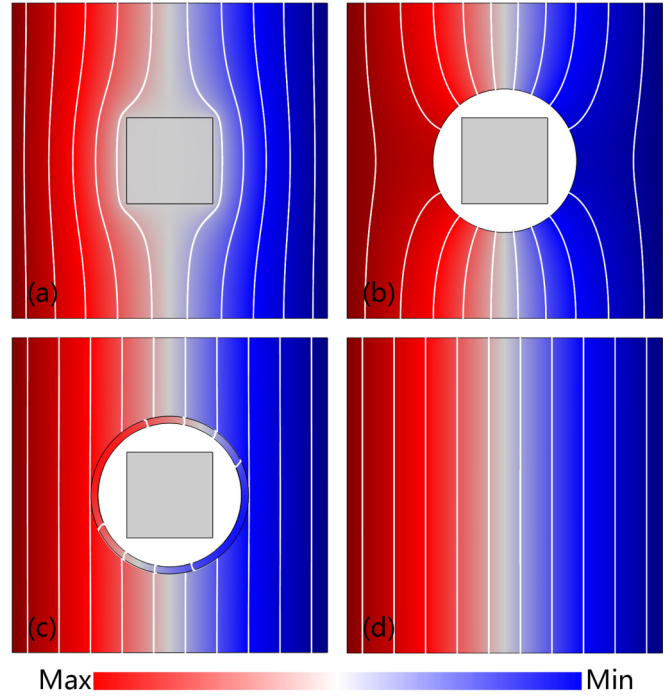, the isolines are contracted [see Fig. 5(b)]. Then, we apply the second layer with two moving rings. In view of the design of bilayer thermal cloaks [30–36], if we enhance the diffusivity of the intermediate layer up to $D'_m = D_m(1 + r^2/r'^2)/(1 - r^2/r'^2)$ (where $r$ and $r'$ are, respectively, the inner and outer radii of the moving rings, and $D'_m$ is enhanced diffusivity), cloaking effect can be achieved. For this purpose, we set the velocity of two moving rings at 37 $\mu$m/s, and the enhanced diffusivity can just satisfy the requirement of a bilayer cloak. As a result, cloaking effect is realized [see Fig. 5(c)], which has the same background concentration profile as a pure background [see Fig. 5(d)].

Cloaking effect still holds when we apply a nonlinear field (see Fig. 6). If there is an object or only one layer for isolation in the center, concentration profiles are distorted [see Figs. 6(a) and 6(a)]. When the bilayer scheme is applied, cloaking effect is obtained again [see Figs. 6(c) and 6(d)]. Therefore, the present scheme is applicable for both linear and nonlinear fields. Actually, one can place any object in the cloaked region without distorting the concentration profile in the background. Such a scheme can avoid anisotropic, singular, and inhomogeneous parameters derived from transformation theory [5–10]. Meanwhile, cloak-on and cloak-off can be easily controlled by velocity.

## IV. DISCUSSION AND CONCLUSION

Incidentally, all parameters adopted in the above simulations are chosen to match practical conditions. For example,
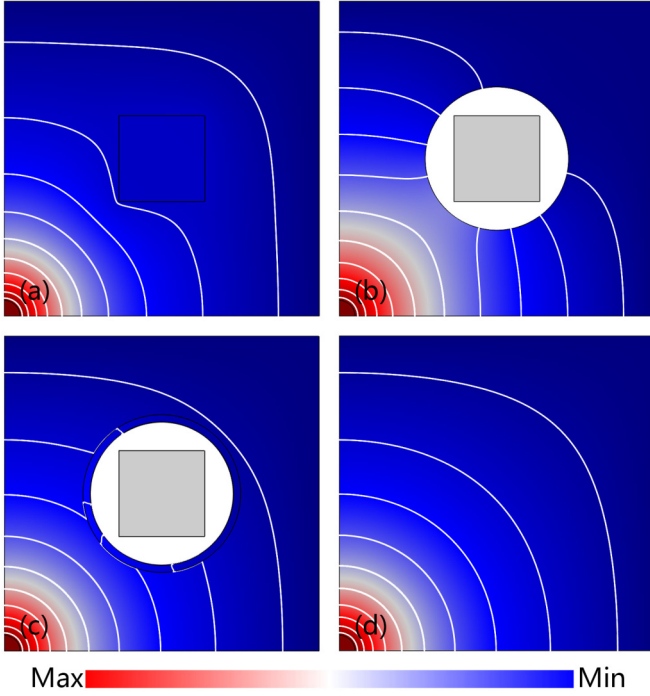
FIG. 6. Cloaking effect in a nonlinear field. The parameters are the same as those for Fig. 5. Differently, a high concentration is set at the left-bottom corner, and a low concentration is set at the upper and right boundaries.

the diffusivity of the two moving rings is approximately set at the magnitude of pure gas diffusion, and that of the intermediate layer is around the magnitude of gas diffusion in a porous medium. A larger porosity means a stronger exchange rate because gas can penetrate between the two moving rings with a higher efficiency. Additionally, the gas in the rings can be driven to rotate by connecting rotary motors to the rings.

In summary, in addition to existing systems, macroscopic particle-diffusion systems can also exhibit exceptional points and geometric phases. We also design a bilayer particle-diffusion cloak with the present structure. These properties may lay a foundation for studying topologically protected phenomena, i.e., by designing the particle-diffusion counterparts of quantum Hall effects or topological insulators/superconductors. Many relevant open questions can be immediately prompted, say, those related to the ion-exchange behavior between membranes or to the manipulation of particle diffusion.

## APPENDIX

We study a two-dimensional model as shown in Fig. 7(a). The perimeter and width of the two moving rings are $l$ and $w$, respectively. The particles in the upper and lower rings move with equal-but-opposite velocities ($+u$ and $-u$). A stationary permeable layer separates the two moving rings, whose thickness ($d$) and diffusivity ($D_m$) determine the exchange rate of particles between the two moving rings. We respectively denote the particle concentrations in the upper ring, lower ring, and intermediate layer as $C_1$, $C_2$, and $C_m$, and the macroscopic particle-diffusion process is dominated by

$$\frac{\partial C_1}{\partial t} = D\left(\frac{\partial^2 C_1}{\partial x^2} + \frac{\partial^2 C_1}{\partial z^2}\right) - u\frac{\partial C_1}{\partial x}, \quad d/2 \leqslant z \leqslant w + d/2$$

$$\frac{\partial C_m}{\partial t} = D_m\left(\frac{\partial^2 C_m}{\partial x^2} + \frac{\partial^2 C_m}{\partial z^2}\right), \quad -d/2 < z < d/2$$

$$\frac{\partial C_2}{\partial t} = D\left(\frac{\partial^2 C_2}{\partial x^2} + \frac{\partial^2 C_2}{\partial z^2}\right) + u\frac{\partial C_2}{\partial x},$$
$$-w - d/2 \leqslant z \leqslant -d/2. \quad \text{(A1)}$$

Equation (A1) indicates the mass conservation of the macroscopic particle-diffusion process. Such a process can be understood by a double-porosity model [16,17] to some extent.

Since we discuss a quasi-one-dimensional system ($l \gg w$ and $l \gg d$), it is reasonable to suppose that the concentration variance along $z$ axis (i.e., $\partial^2 C/\partial z^2$) is negligible. We set the intermediate layer to be thin enough, and the middle equation in Eq. (A1) can be treated as two particle sources ($s_1$ for the upper ring and $s_2$ for the lower ring). Then, Eq. (A1) can be reduced to

$$\frac{\partial C_1}{\partial t} = D\frac{\partial^2 C_1}{\partial x^2} - u\frac{\partial C_1}{\partial x} + s_1, \quad d/2 \leqslant z \leqslant w + d/2$$

$$\frac{\partial C_2}{\partial t} = D\frac{\partial^2 C_2}{\partial x^2} + u\frac{\partial C_2}{\partial x} + s_2, \quad -w - d/2 \leqslant z \leqslant -d/2. \quad \text{(A2)}$$

Boundary conditions are given by the continuities of particle concentrations and particle fluxes,

$$C_1 = C_m, \quad z = d/2$$
$$C_2 = C_m, \quad z = -d/2$$
$$j_1 = -D\frac{\partial C_1}{\partial z} = -D_m\frac{\partial C_m}{\partial z}, \quad z = d/2$$
$$j_2 = D\frac{\partial C_2}{\partial z} = D_m\frac{\partial C_m}{\partial z}, \quad z = -d/2, \quad \text{(A3)}$$

where $j_1$ and $j_2$ are the particle fluxes from the intermediate layer to the upper and lower rings, respectively. Since we have neglected the higher-order terms ($\partial^2 C/\partial z^2 = 0$), $C_m$ is linear along $z$ axis, thus yielding $\partial C_m/\partial z = (C_1 - C_2)/d$. Since the width of the two moving rings $w$ is thin enough, we can assume that the particle sources are uniformly distributed, say, $s_1 = j_1/w = -D_m(C_1 - C_2)/wd = -s_2$. Then, Eq. (A2) can
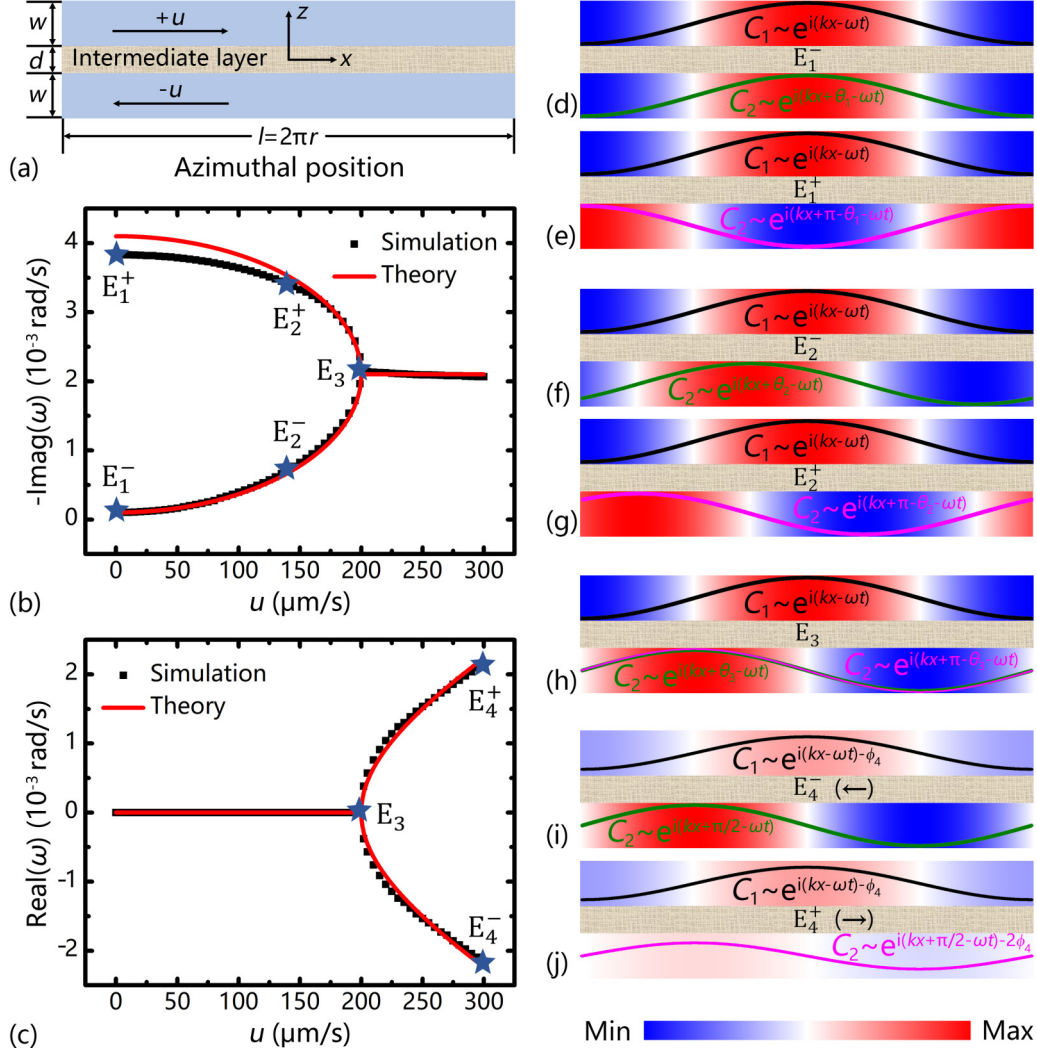
FIG. 7. Eigenvalues and eigenstates. (a) Simplified two-dimensional model with $r = 10$ cm, $w = 0.5$ cm, $d = 0.1$ cm, $D = 10^{-6}$ m$^2$/s, and $D_m = 10^{-8}$ m$^2$/s. (b) Negative imaginary part and (c) real part of the eigenvalue $\omega$ as a function of velocity $u$. Solid lines and block squares are analytical results and simulation results, respectively. (d)–(j) Eigenstates at different positions indicated by stars in (b) and (c).

be further reduced to

$$\frac{\partial C_1}{\partial t} = D\frac{\partial^2 C_1}{\partial x^2} - u\frac{\partial C_1}{\partial x} + h(C_2 - C_1),$$
$$d/2 \leqslant z \leqslant w + d/2$$
$$\frac{\partial C_2}{\partial t} = D\frac{\partial^2 C_2}{\partial x^2} + u\frac{\partial C_2}{\partial x} + h(C_1 - C_2),$$
$$-w - d/2 \leqslant z \leqslant -d/2, \qquad (A4)$$

where $h = D_m/(w\,d)$ reflects particle exchange rate. When $D_m$ is small, the particle exchange between the two moving rings has time delay, thus yielding a small exchange rate $h$. Although Eq. (A4) typically describes a diffusion process (characterized by a first-order partial derivative with respect to time $t$), we use plane-wave solutions to handle the diffusion process,

$$C_1 = A_1 e^{i(kx-\omega t)} + B_1$$
$$C_2 = A_2 e^{i(kx-\omega t)} + B_2, \qquad (A5)$$

where $A_1$ (or $A_2$) and $B_1$ (or $B_2$) are the amplitude and reference value of the particle concentration in the upper (or lower) ring, respectively. This is reasonable because we apply a periodic boundary condition. We neglect the reference values (say, $B_1 = B_2 = 0$) for brevity, and care about the real parts of Eq. (A5) only. The substitution of Eq. (A5) into Eq. (A4) yields

$$\omega A_1 = -ik^2 D A_1 + kuA_1 + ih(A_2 - A_1),$$
$$d/2 \leqslant z \leqslant w + d/2$$
$$\omega A_2 = -ik^2 D A_2 - kuA_2 + ih(A_1 - A_2),$$
$$-w - d/2 \leqslant z \leqslant -d/2. \qquad (A6)$$

Equation (A6) can be rewritten as an eigenequation $\boldsymbol{H\psi} = \omega\boldsymbol{\psi}$ where $\boldsymbol{H}$ has the form of Eq. (1) in the main text.

We also plot the real and imaginary parts of eigenvalues in the $u$-space, as illustrated in Figs. 7(b) and 7(c). In the region $u < u_{\mathrm{EP}}$, $\boldsymbol{H}$ occupies two branches of purely imaginary eigenvalues, and the system is in an anti-parity-time

symmetric region [21]. Especially, right at the exceptional point $u = u_{EP}$, the system marks the merging of two eigenvalues. When $u > u_{EP}$, the real part of eigenvalue appears due to the broken of anti-parity-time symmetry. Therefore, this point $u_{EP} = h/k$ serves as an exceptional point of velocity.

For a vanishing exchange rate ($h = 0$), the eigenvalue always possess nonzero real parts at $u \neq 0$, so there is only a moving state. That is, the two concentration profiles in the upper and lower rings propagate independently. Differently, when the two rings are coupled together ($h \neq 0$), the system exhibits two different states as $u$ varies. Therefore, the particle exchange between the two moving rings is a key factor, which can be regarded as the interference of the macroscopic particle-diffusion system. When $u < h/k$, eigenvalues are purely imaginary. Therefore, the concentration profiles in the two moving rings maintain a constant phase difference ($\pi - \theta$ for $\omega_+$ and $\theta$ for $\omega_-$), and decay motionlessly. When $u > h/k$, the real parts of eigenvalues appear. Thus, the concentration profiles in the two moving rings maintain a constant phase difference ($\pi/2$ for both $\omega_+$ and $\omega_-$), but decay with motion.

We also perform finite-element simulations to confirm the approximation from Eqs. (A1) to (A2). Due to the periodic boundary condition, the two moving rings with length $l = 2\pi r$ only allow discrete wave numbers $k = nl/2\pi = nr^{-1}$ with $n$ being any positive integers. We focus on the fundamental modes ($n = 1$) which have the lowest decay rate. The simulation eigenvalues are obtained by setting the initial states to be exactly the corresponding eigenstates,

say, $C_1(x, t = 0) = A_1 \cos(kx) + B_1$ and $C_2(x, t = 0) = A_2 \cos(kx + \theta) + B_2$ corresponding to $\omega_-$ [or $C_2(x, t = 0) = A_2 \cos(kx + \pi - \theta) + B_2$ corresponding to $\omega_+$] with $A_1 = A_2 = 200$, $B_1 = B_2 = 300$, and $\theta = \sin^{-1}(ku/h)$. We fit the amplitude decaying from 250 to 60000 s with the function of $C = Ae^{-\lambda t} + B$, where $\lambda = -\text{Im}(\omega)$ is decay rate. When the velocity exceeds the exceptional point, we also track the motion before 2000 s and calculate the frequency [Real($\omega$)]. The simulation results are plotted as discrete dots in Figs. 7(b) and 7(c), which agree with the solid lines predicted by Eq. (2). Since the eigenstates at the upper branch have larger decay rates, they are metastable, resulting in smaller simulation eigenvalues of $-\text{Im}(\omega)$ than theoretical ones.

We also plot the eigenstates indicated by the stars in Figs. 7(b) and 7(c) [see Figs. 7(d)–7(j)]. When plotting the eigenstates, we adjust the length $l$ and width $w$ to keep an appropriate ratio for the clarity of presentation. When $u = 0$, the phase differences are $\theta_1 = 0$ for eigenstate $E_1^-$ and $\pi - \theta_1 = \pi$ for eigenstate $E_1^+$. As $u$ increases to the exceptional point, $\theta = \sin^{-1}(ku/h)$ also increases to $\pi/2$. Thus, the two profiles of $C_1$ and $C_2$ coincide with each other with a phase difference of $\pi/2$. The eigenstates in Figs. 7(d)–7(h) decay motionlessly. When $u > u_{EP}$, the concentration profiles keep a phase difference of $\pi/2$ and propagate together. The direction follows the moving ring with a larger concentration amplitude, i.e., backward in Fig. 7(i) and forward in Fig. 7(j). The finite-element simulations agree with the eigenstates predicted by Eqs. (3) and (4).

---

[1] C. A. Mead and D. G. Truhlar, On the determination of Born-Oppenheimer nuclear motion wave functions including complications due to conical intersections and identical nuclei, J. Chem. Phys. **70**, 2284 (1979).

[2] C. Z. Ning and H. Haken, Geometrical Phase and Amplitude Accumulations in Dissipative Systems with Cyclic Attractors, Phys. Rev. Lett. **68**, 2109 (1992).

[3] P. T. Callaghan, A. Coy, D. MacGowan, K. J. Packer, and F. O. Zelaya, Diffraction-like effects in NMR diffusion studies of fluids in porous solids, Nature **351**, 467 (1991).

[4] D. S. Grebenkov, NMR survey of reflected Brownian motion, Rev. Mod. Phys. **79**, 1077 (2007).

[5] S. Guenneau and T. M. Puvirajesinghe, Fick's second law transformed: One path to cloaking in mass diffusion, J. R. Soc. Interface **10**, 20130106 (2013).

[6] S. Guenneau, D. Petiteau, M. Zerrad, C. Amra, and T. Puvirajesinghe, Transformed Fourier and Fick equations for the control of heat and mass diffusion, AIP Adv. **5**, 053404 (2015).

[7] J. M. Restrepo-Florez and M. Maldovan, Mass separation by metamaterials, Sci. Rep. **6**, 21971 (2016).

[8] J. M. Restrepo-Florez and M. Maldovan, Rational design of mass diffusion metamaterial concentrators based on coordinate transformations, J. Appl. Phys. **120**, 084902 (2016).

[9] J. M. Restrepo-Florez and M. Maldovan, Mass diffusion cloaking and focusing with metamaterials, Appl. Phys. Lett. **111**, 071903 (2017).

[10] J. M. Restrepo-Florez and M. Maldovan, Metamaterial membranes, J. Phys. D: Appl. Phys. **50**, 025104 (2017).

[11] C. Z. Fan, Y. Gao, and J. P. Huang, Shaped graded materials with an apparent negative thermal conductivity, Appl. Phys. Lett. **92**, 251907 (2008).

[12] T. Y. Chen, C.-N. Weng, and J.-S. Chen, Cloak for curvilinearly anisotropic media in conduction, Appl. Phys. Lett. **93**, 114103 (2008).

[13] L. J. Xu, S. Yang, and J. P. Huang, Dipole-assisted thermotics: Experimental demonstration of dipole-driven thermal invisibility, Phys. Rev. E **100**, 062108 (2019).

[14] L. J. Xu, G. L. Dai, and J. P. Huang, Transformation Multithermotics: Controlling Radiation and Conduction Simultaneously, Phys. Rev. Appl. **13**, 024063 (2020).

[15] J. P. Huang, Thermal metamaterials make it possible to control the flow of heat at will, ES Energy Environ. **6**, 1 (2019).

[16] G. I. Barenblatt and I. P. Zheltov, Basic concepts in the theory of seepage of homogeneous liquids in fissured rocks, J. Appl. Math. Mech. **24**, 1286 (1960).

[17] G. I. Barenblatt and Yu. P. Zheltov, Fundamental equations of filtration of homogeneous liquids in fissured rocks, Dokl. Akad. Nauk SSSR **132**, 545 (1960) [Sov. Phys. Dokl. **5**, 522 (1960)].

[18] R. Fleury, D. L. Sounas, C. F. Sieck, M. R. Haberman, and A. Alu, Sound isolation and giant linear nonreciprocity in a compact acoustic circulator, Science **343**, 516 (2014).

[19] D. Torrent, O. Poncelet, and J. C. Batsale, Nonreciprocal Thermal Material by Spatiotemporal Modulation, Phys. Rev. Lett. **120**, 125501 (2018).

[20] Y. Li, K. J. Zhu, Y. G. Peng, W. Li, T. Z. Yang, H. X. Xu, H. Chen, X. F. Zhu, S. H. Fan, and C. W. Qiu, Thermal

meta-device in analogue of zero-index photonics, Nat. Mater. **18**, 48 (2019).

[21] Y. Li, Y. G. Peng, L. Han, M. A. Miri, W. Li, M. Xiao, X. F. Zhu, J. L. Zhao, A. Alu, S. H. Fan, and C. W. Qiu, Anti-parity-time symmetry in diffusive systems, Science **364**, 170 (2019).

[22] P. C. Cao, Y. Li, Y. G. Peng, C. W. Qiu, and X. F. Zhu, High-order exceptional points in diffusive systems: Robust APT symmetry against perturbation and phase oscillation at APT symmetry breaking, ES Energy Environ. **7**, 48 (2020).

[23] J. H. Wu, M. Artoni, and G. C. La Rocca, Parity-time-antisymmetric atomic lattices without gain, Phys. Rev. A **91**, 033811 (2015).

[24] P. Peng, W. X. Cao, C. Shen, W. Z. Qu, J. M. Wen, L. Jiang, and Y. H. Xiao, Anti-parity–time symmetry with flying atoms, Nat. Phys. **12**, 1139 (2016).

[25] F. Yang, Y. C. Liu, and L. You, Anti-PT symmetry in dissipatively coupled optical systems, Phys. Rev. A **96**, 053845 (2017).

[26] Y. Choi, C. Hahn, J. W. Yoon, and S. H. Song, Observation of an anti-PT-symmetric exceptional point and energy-difference conserving dynamics in electrical circuit resonators, Nat. Commun. **9**, 2182 (2018).

[27] V. V. Konotop and D. A. Zezyulin, Odd-Time Reversal PT Symmetry Induced by An Anti-PT-Symmetric Medium, Phys. Rev. Lett. **120**, 123902 (2018).

[28] J. C. Garrison and E. M. Wright, Complex geometrical phases for dissipative systems, Phys. Lett. A **128**, 177 (1988).

[29] A. A. Mailybaev, O. N. Kirillov, and A. P. Seyranian, Geometric phase around exceptional points, Phys. Rev. A **72**, 014104 (2005).

[30] H. Y. Xu, X. H. Shi, F. Gao, H. D. Sun, and B. L. Zhang, Ultrathin Three-Dimensional Thermal Cloak, Phys. Rev. Lett. **112**, 054301 (2014).

[31] T. C. Han, X. Bai, D. L. Gao, J. T. L. Thong, B. W. Li, and C.-W. Qiu, Experimental Demonstration of a Bilayer Thermal Cloak, Phys. Rev. Lett. **112**, 054302 (2014).

[32] Y. G. Ma, Y. C. Liu, M. Raza, Y. D. Wang, and S. L. He, Experimental Demonstration of a Multiphysics Cloak: Manipulating Heat Flux and Electric Current Simultaneously, Phys. Rev. Lett. **113**, 205501 (2014).

[33] Y. X. Liu, W. L. Guo, and T. C. Han, Arbitrarily polygonal transient thermal cloaks with natural bulk materials in bilayer configurations, Int. J. Heat Mass Transfer **115**, 1 (2017).

[34] T. C. Han, P. Yang, Y. Li, D. Y. Lei, B. W. Li, K. Hippalgaonkar, and C.-W. Qiu, Full-parameter omnidirectional thermal metadevices of anisotropic geometry, Adv. Mater. **30**, 1804019 (2018).

[35] J. Qin, W. Luo, P. Yang, B. Wang, T. Deng, and T. C. Han, Experimental demonstration of irregular thermal carpet cloaks with natural bulk material, Int. J. Heat Mass Transfer **141**, 487 (2019).

[36] L. J. Xu and J. P. Huang, Metamaterials for Manipulating Thermal Radiation: Transparency, Cloak, and Expander, Phys. Rev. Appl. **12**, 044048 (2019).